

# FFT modelling of high resolution XRD peaks with a discrete Green operator and a sub-voxelization method.

K. S. ELOH<sup>a,b</sup>, A. JACQUES<sup>a</sup>, S. BERBENNI<sup>b</sup>

a. IJL, CNRS / Université de Lorraine, 2 allée André Guinier, 54011 Nancy, France -

[komlavi-senyo.eloh@univ-lorraine.fr](mailto:komlavi-senyo.eloh@univ-lorraine.fr)

b. LEM3, CNRS / Université de Lorraine, 7 Rue Félix Savart, 57073 Metz, France –

[stephane.berbenni@univ-lorraine.fr](mailto:stephane.berbenni@univ-lorraine.fr)

## Résumé :

*La construction de sources synchrotron de rayons X a permis l'étude in situ et en temps réel des matériaux sous chargements mécaniques et/ou transformation de phase. Ces expériences produisent des milliers de diagrammes de diffraction 2D dont l'analyse n'est pas triviale car elles résultent de l'effet conjugué des défauts microstructuraux, des contraintes internes et des chargements mécaniques. La modélisation numérique des diagrammes de diffraction est donc nécessaire. Elle consiste à évaluer les champs mécaniques (champs de déformations ou de déplacements) dans un matériau et à générer les diagrammes théoriques correspondant à cet état de contraintes. La précision de cette modélisation est liée à celle de la méthode numérique utilisée pour calculer les champs mécaniques. Pour simuler les diagrammes théoriques, nous utilisons une méthode micromécanique basée sur l'algorithme FFT pour calculer le champ de déplacements dans un matériau de structure périodique. Pour améliorer la précision de cette méthode, nous introduisons un opérateur de Green discret et une méthode de sous-voxélisation pour la suppression des oscillations numériques et des artéfacts numériques. Nous montrons l'effet de ces défauts numériques sur les diagrammes de diffraction et appliquons le modèle pour étudier des cas de référence comme des boucles de dislocations parfaites et partielles, ou encore une répartition aléatoire de boucles de dislocations.*

## Abstract:

*Synchrotron X-ray now allows to study in situ and in real time the mechanical behavior of materials under loading and/or phase transformation. Such experiments result in thousands 2D diffraction patterns. However, the analysis of these images is not an easy task because they are sensitive to microstructural defects, internal stresses and applied load. An alternative method to complete this study is the forward modeling of the diffraction patterns. In this numerical method, we first need to compute the mechanical fields (strain or displacement fields) in a deformed material. The computed field is then used to generate theoretical X-ray diffraction peaks, which are compared to experimental results. The quality of the forward modeling method strongly depends on the accuracy of the numerical method used to compute the mechanical fields. In the present paper, a micromechanical method based on the FFT algorithm is used to compute the displacement field. To improve this spectral method, we develop a discrete Green operator to suppress numerical oscillations and a sub-voxelization method to remove artifacts on the displacement field. Throughout numerical examples, we show the effect of these numerical defects on the simulated peaks and finally our numerical model is used to study some reference cases such as perfect or faulted dislocation loops, or a random distribution of dislocation loops.*

**Mots clefs : Transformée de Fourier rapide, Opérateur de Green, sous-voxélisation, simulation de pics de diffraction.**

## 1 Introduction

Since the advent of powerful synchrotron X-Ray sources and fast 2D X-Ray detectors, *in situ* experiments on materials during phase transformations or mechanical testing [1–5] result in terabytes of data (i.e. tens of thousands of images). These data need to be processed in order to retrieve useful information on the material's state. However, while the relation between the variations of diffraction peaks positions (the  $2\theta_B$  Bragg angle) can be related to variations in average strain, the effect of the microstructure (size of the diffraction volumes, defect content...) on the peaks shapes (width, slope...) is less obvious and can be known only in simple cases [6–8]. An alternate possibility called forward modeling is to compute the elastic fields (strain, displacement) expected from a representative volume of material with a given microstructure and stress state, then to generate theoretical diffraction peaks and compare those with experimental ones [9–14]. As several material parameters (defect density, phases and stress distribution...) need to be considered and a real microstructure may be quite complex, this is a computer intensive technique, and its practicability depends on the accuracy and the efficiency of the numerical method used to compute the mechanical field.

Numerical methods based on Fast Fourier Transform (FFT) are increasingly used to compute mechanical fields in a material with a periodic and voxelized microstructure [15–19]. These spectral methods have many advantages: they are easy to implement, they have a good accuracy and the computational time is low compared to the Finite Element Method (FEM) for a same number of degrees of freedom. They were introduced by Moulinec and Suquet [15,16] to compute the effective mechanical behavior of linear elastic composites and are currently used for many mechanical problems. However, the computed elastic fields exhibit numerical oscillations close to discontinuities such as phase boundaries or dislocation loops [15,20]. As seen below, such oscillations result in phantom peaks in the simulated diffracted intensity, which may mask real physical effects.

These oscillations have three sources: the classical Gibbs phenomenon, aliasing and microstructure voxelization. Unfortunately, they cannot be smoothed out by simple techniques such as the use of low pass filters, as these would add other phantom peaks.

In the present paper, we show that unwanted oscillations can be removed by using both a modified *discrete* Green operator in the computation of the elastic fields and a “sub-voxelization” method to remove the voxelization effect [20,21]. We then show the effect of these corrections on the computed diffraction intensities for a f.c.c. material containing a single perfect or faulted dislocation loop.

## 2 FFT modeling of diffraction peaks

Under kinematical conditions and assuming a coherent beam, the amplitude of a diffracted wave at a position  $\mathbf{G} + \mathbf{q}$  in the vicinity of a reciprocal  $\mathbf{G}$  lattice vector is [9,10,22–24] :

$$A(\mathbf{q}) = FT[A_0(\mathbf{r}) \times F(\mathbf{G}, \mathbf{x}) \times \exp(-2i\pi \mathbf{G} \cdot \mathbf{u}(\mathbf{x}))] \quad (1)$$

where  $\mathbf{x}$  is the position of the scattering atom,  $A_0(\mathbf{x})$  is the amplitude of the incident electromagnetic wave,  $F(\mathbf{G}, \mathbf{x})$  is the local structure factor and  $\mathbf{u}(\mathbf{x})$  the displacement field. The scattered intensity is  $I(\mathbf{q}) = |A(\mathbf{q})|^2$ .

In order to compute the displacement field, we take the material as a periodic repetition of a cubic Representative Volume Element divided in  $n^3$  voxels (we usually take  $n = 512$ ). In this paper, for simplicity we assume linear homogeneous elasticity with an eigenstrain field  $\boldsymbol{\varepsilon}^*$  and a homogeneous linear elastic stiffness tensor  $\mathbf{c}^0$ . Using the Green's function technique, the displacement field due to eigenstrains is given at every position by (see e.g. [25]):

$$\mathbf{u}(\mathbf{x}) = \mathbf{u}_o + (\mathbf{B} * \mathbf{c}^0 : \boldsymbol{\varepsilon}^*)(\mathbf{x}) \quad (2)$$

$\mathbf{u}_o$  is an imposed displacement field (which is not considered in the paper), the symbol  $*$  denotes the spatial convolution product and  $\mathbf{B}$  is the third order Green operator associated with periodic boundary conditions. The first term will define the average diffraction peak position and the second the distribution of the scattered intensity around this position. In Fourier space this equation becomes:

$$\hat{\mathbf{u}}(\boldsymbol{\xi}) = \hat{\mathbf{B}}(\boldsymbol{\xi}) : \mathbf{c}^0 : \hat{\boldsymbol{\varepsilon}}^*(\boldsymbol{\xi}) \quad (3)$$

The Fourier transform  $\hat{\mathbf{B}}$  of  $\mathbf{B}$  is given as function of the Fourier transform of the elastic Green function  $\hat{\mathbf{G}}$  by [25]:

$$\hat{B}_{ijk}(\boldsymbol{\xi}) = \frac{i}{2} (\hat{G}_{ij}\xi_k + \hat{G}_{ik}\xi_j) \quad (4)$$

The eigenstrain tensor  $\boldsymbol{\varepsilon}^*$  can be due to local variations of the lattice parameter (different phases or an uneven distribution of impurities) and to crystal defects such as dislocations loops. In this paper, we focus on the latter as they involve displacement discontinuities. A dislocation loop is voxelized as a planar, one voxel thick, transformed platelet surrounded by the dislocation. The eigenstrain is homogeneous within the voxel volume, which must be much larger than the lattice cell volume. The eigenstrain tensor of the transformed voxels is given by [26,27]:

$$\varepsilon_{ij}^* = \frac{1}{2d} (n_i b_j + n_j b_i) \quad (5)$$

where  $(n_1, n_2, n_3)$  are the Miller indices of the plane which has slipped by a relative amount  $\mathbf{b}(b_1, b_2, b_3)$  and  $d$  is the voxel size.

### 3 Improvement of the displacement field computation

#### 3.1 Discrete Green operator for displacement field

Let us consider a rectangular dislocation loop perpendicular to the z-axis with a Burgers vector  $\mathbf{b}(0, 0, b_3)$  in a homogeneous isotropic material (Young's modulus  $E = 333.4 \text{ GPa}$  and the Poisson ratio  $\nu = 0.26$ ). This approximately corresponds to the room temperature elastic constants of a single crystalline Ni-based Superalloy. The dislocation loop is a square-shaped inclusion with an eigenstrain tensor defined as:  $\varepsilon_{ij}^* = 0$  except  $\varepsilon_{33}^* = 1$ . The unit cell is discretized in  $128 \times 128 \times 128$  voxels and the platelet inclusion size for the dislocation is  $32 \times 32 \times 1$ . Figure 1 (left) shows the displacement fields along z-axis due to this dislocation loop.

Some oscillations appear close to the dislocation loop. These numerical oscillations can be related to the aliasing phenomenon. Numerical examples show that these numerical oscillations are due to the classical Green operator used in the initial method [15,16]. To correct these numerical oscillations, we develop a new expression  $\hat{\mathbf{B}}'$  of the Fourier transform of the Green's operator using an efficient discretization of the real space [20]:

$$\hat{\mathbf{B}}'(\xi_{ijk}) = A_{ijk} \sum_{m,n,p=-\infty}^{+\infty} \frac{(-1)^{m+n+p}}{(mN+i)} \frac{1}{(nN+j)} \frac{1}{(pN+k)} \hat{\mathbf{B}}(\xi_{mN+i, nN+j, pN+k}) \quad (6)$$

$$\text{With} \quad A_{ijk} = \left(\frac{N}{\pi}\right)^3 \sin\left(\frac{i\pi}{N}\right) \sin\left(\frac{j\pi}{N}\right) \sin\left(\frac{k\pi}{N}\right)$$

The discrete  $\hat{\mathbf{B}}'(\xi_{ijk})$  operator used to compute the displacement field as well as the discrete  $\hat{\mathbf{F}}'(\xi_{ijk})$  operator [20] used to compute the strain field have nearly the same form as the discrete  $\hat{\mathbf{F}}'(\xi_{ijk})$  operator reported by Brisard and Dormieux [28]. They are both modulated by Sinc functions but in [28] the Sinc functions are squared because these authors used the Hashin-Shtrikmann variational principle, which is different from our integral formulation.

Figure 1 (right) shows the displacement field computed using the proposed discrete Green operator (for  $m = n = p \in [-21, 20]$ ). The numerical oscillations are removed.

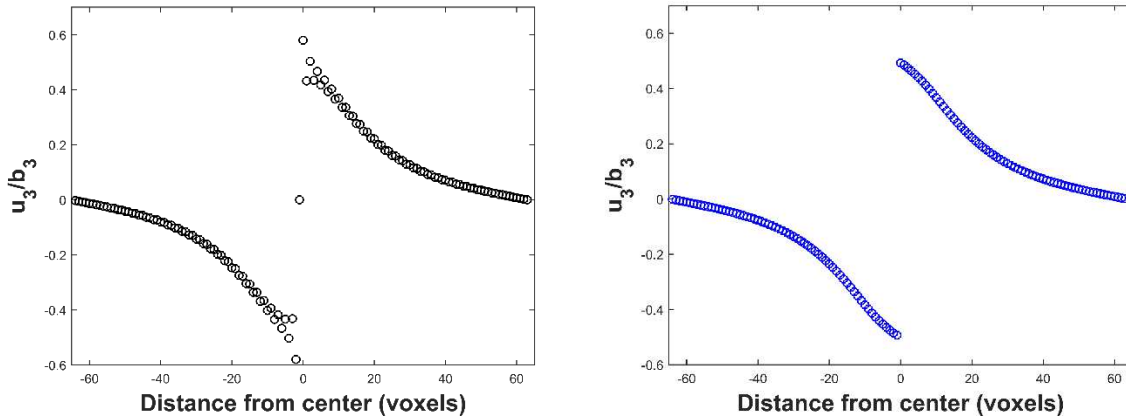


*Figure 1* Displacement field due to a rectangular dislocation loop. On the left, the displacement field is computed using the classical Green operator and on the right side, the displacement field is computed using the proposed discrete Green operator. The oscillations are suppressed. The center point was also shifted by  $b/2$ .

### 3.2 Sub-voxelization

Let us now consider a hexagonal dislocation loop with a Burgers vector  $\mathbf{b} = \frac{a}{2}[0\bar{1}1]$  lying in a (111) slip plane of a f.c.c. crystal. The material is discretized in  $512 \times 512 \times 512$  voxels. This hexagonal dislocation loop consists of two screw dislocation segments and six  $60^\circ$  dislocation segments. Figure (2a) shows the displacement field along a line in the  $z$  direction crossing the dislocation loop. The displacement is zero in the voxel  $r_i$  belonging to the dislocation loop (it should be  $\pm \frac{b}{2}$ ), and oscillates in the neighboring voxels  $\dots r_{i-3}, r_{i-2}, r_{i-1}, r_{i+1}, r_{i+2}, r_{i+3} \dots$ . These damped oscillations obviously result from the voxelization of the dislocation loop plane (figure (2c)), and would disappear at these points for a finer discretization  $(512 \times m)^3$  (figure (2d)). We can thus define a ‘‘patch’’  $\Delta_k(r_j - r_i)$  which is the difference between the  $k$  component of the displacement computed with a  $(512 \times m)^3$  grid and the initial  $512^3$  grid:

$$\Delta_k(r_j - r_i) = u_k^{sub}(r_j - r_i) - u_k^{init}(r_j - r_i) \quad (7)$$

The computation method for  $\Delta_k$  is detailed in Eloh et al. [21]. The correction is finite for voxels in the neighborhood of  $r_j$  and negligible at far distances. The total correction is then the convolution of  $\Delta_k$  (including a  $\frac{b}{2}$  shift) and the voxelated eigenstrain field. The result is shown in figure (2b): the displacement field exhibits a jump of size  $b = a/2$  at the dislocation loop plane. It is now continuous modulo a crystal lattice vector, and the phase shift  $\mathbf{G} \cdot \Delta \mathbf{u}(\mathbf{x})$  (equation (1)) is an integer number.

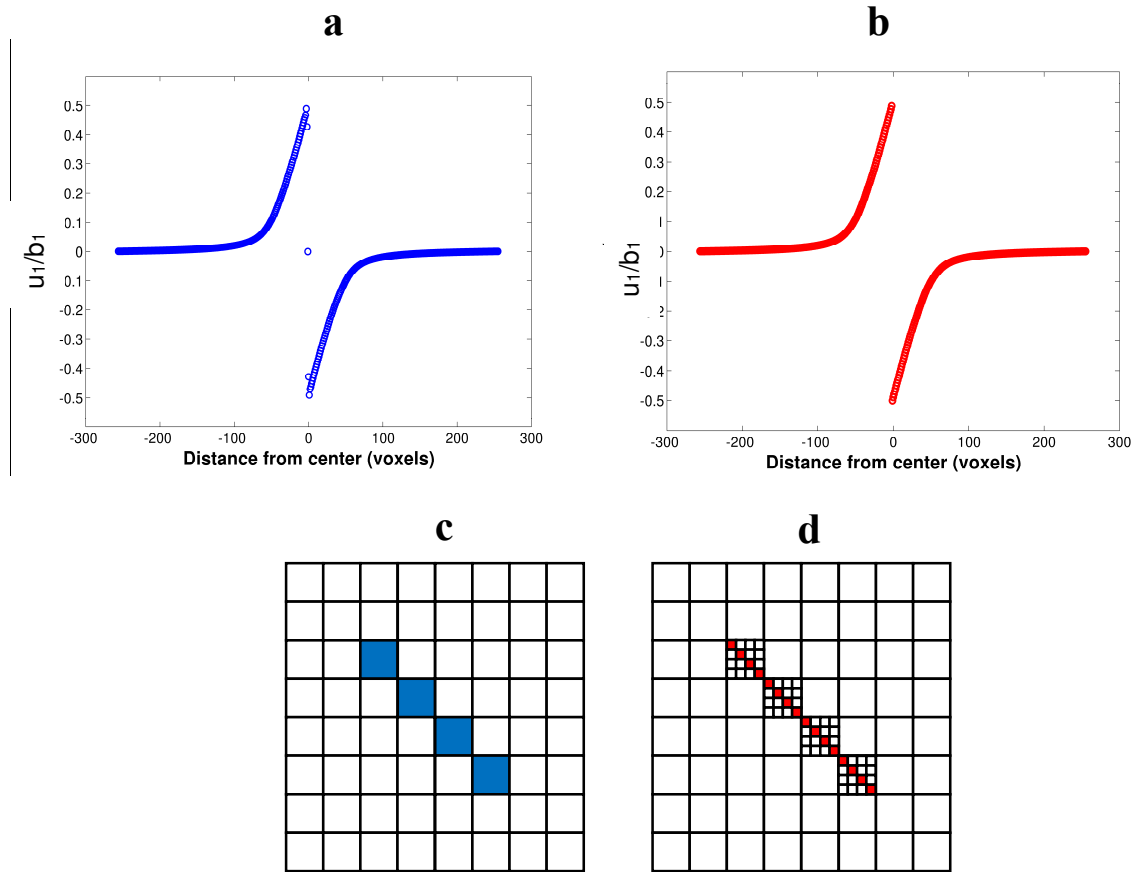
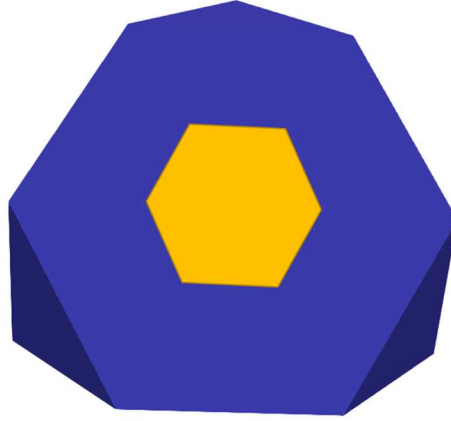


Figure 2 : (a) Displacement field due to a hexagonal dislocation loop showing artifacts close to the dislocation loop. These artifacts result from the voxelisation of the dislocation loop represented in (c). Mimicking a finer voxelisation (d), we computed a patch  $\Delta_k$  which suppresses these artifacts. The corrected displacement field is represented in (b).

## 4 Numerical simulations: perfect and faulted dislocation loops

### 4.1 Perfect hexagonal dislocation loop

In order to test the result of the above corrections, we compute the intensity of the (200) diffraction peak of a representative volume (size:  $1\mu\text{m}^3$  divided into  $512^3$  voxels) containing a single dislocation loop with a  $b = \frac{a}{2}[\bar{1}10]$  Burgers vector lying in a (111) slip plane shown in figure 3. Each segment is  $36\sqrt{2}/512 \mu\text{m}$  long. The corresponding dislocation density is  $\sim 6 \times 10^{11} \text{m}^{-2}$ .



*Figure 3: Hexagonal loop (i.e. transformed platelet) lying in a (111) plane of a f.c.c. crystal used for diffraction peaks simulation.*

The 3D distribution of the diffracted intensity is reported on Figure 4 with an arbitrary logarithmic scale in the (0 $\bar{1}1$ ) (a) and (111) (b) planes containing the (256,256,256) voxel with maximum intensity (about  $10^{16}$ ). The total scattered intensity scales as  $512^6$ . Line 0, 1, and 2 respectively show the peak computed with the classical operator, the present discrete operator (eq. (6)), and after the patch correction (eq. (7) and Fig. 2(b)).

All three peaks share common features: an asymmetric high intensity zone surrounding the central voxel, and low intensity streaks along the [111] direction (0a, 1a, 2a) and the [ $\bar{1}\bar{1}\bar{1}$ ], [ $\bar{1}2\bar{1}$ ], and [ $\bar{1}\bar{1}2$ ] directions (0b, 1b, 2b): each dislocation segment along a  $\langle 110 \rangle$  direction in the loop plane generates a linear highly distorted zones, and the corresponding (Fourier transformed) scattered intensity is distributed in the orthogonal {110} plane which intersects the (0 $\bar{1}1$ ) plane along [111] and the (111) plane along a  $\langle 211 \rangle$  direction. The scattered intensity exhibits oscillations parallel (a) or perpendicular (b) to the streaks. Simulations with different loop sizes (not represented here) showed that the period of these oscillations varies as the inverse of the loop size.

A salient feature of figures 4( $a_0$ ) and 4( $a_1$ ) is a strong streak in direction [111] surrounded by oscillations. In figure 4( $a_0$ ), its intensity is increasing with increasing distance from the center with a maximum in the vicinity of voxel (512,512,512). The intensity is lower and slowly decreasing in figure 4( $a_1$ ). On the contrary, the intensity is strongly decreasing in figure 4( $a_2$ ). Two phantom peaks are also visible in figures 4( $b_0$ ) and 4( $b_1$ ). The authors believe these features are due to a parasitic scattered amplitude resulting from a surface “defect” i.e. fast oscillations of the displacement field in the loop plane and its immediate vicinity: these are oscillations resulting from the classical Green operator and from the voxelization and the point at position  $r_i$ .

## 4.2 Faulted hexagonal dislocation loop

Figure 5 shows the corrected displacement field (Figure 5(a)) and the (200) diffracted intensities (figures 5(b) and 5(c)) for a single loop having the same geometry as figure 3, but with  $\mathbf{b} = \frac{a}{6} [\bar{2}11]$  which corresponds to a stacking fault in the loop plane. The displacement field is nearly the same as in figure 2b with a  $2/3$  scale factor. As a result, the displacement shift in direction x at the loop plane is no longer a crystal lattice translation vector, the  $\mathbf{G} \cdot \mathbf{b}$  scalar product is  $2/3$ , and there is a step in the phase. The Fourier transform of the faulted surface is a line along the [111] direction, and as the Fourier transform of a Heaviside step function is  $q^{-1}$ , we may expect a streak along [111] with an intensity varying as  $q^{-2}$ . This is indeed observed in figure 5(b).

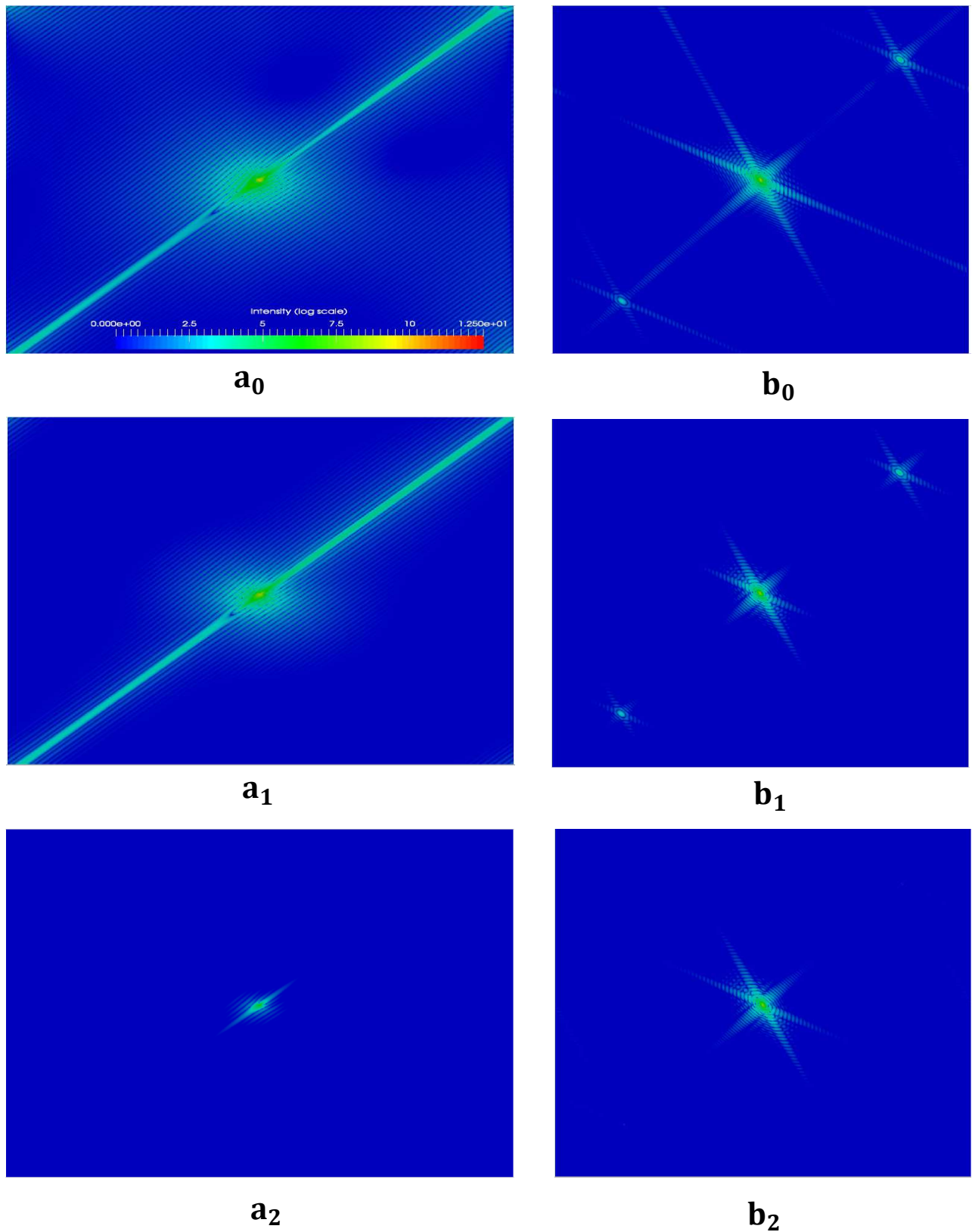


*Figure 4: 2D plots of the diffracted intensities for a single hexagonal dislocation loop deduced from the displacement field computed with the classical operator (0), the discrete operator (1), and after correction (2). The intensities are plotted in the  $(0\bar{1}1)$  plane (Figs.  $a_0, a_1, a_2$ ) and the  $(111)$  plane (Figs.  $b_0, b_1, b_2$ ).*

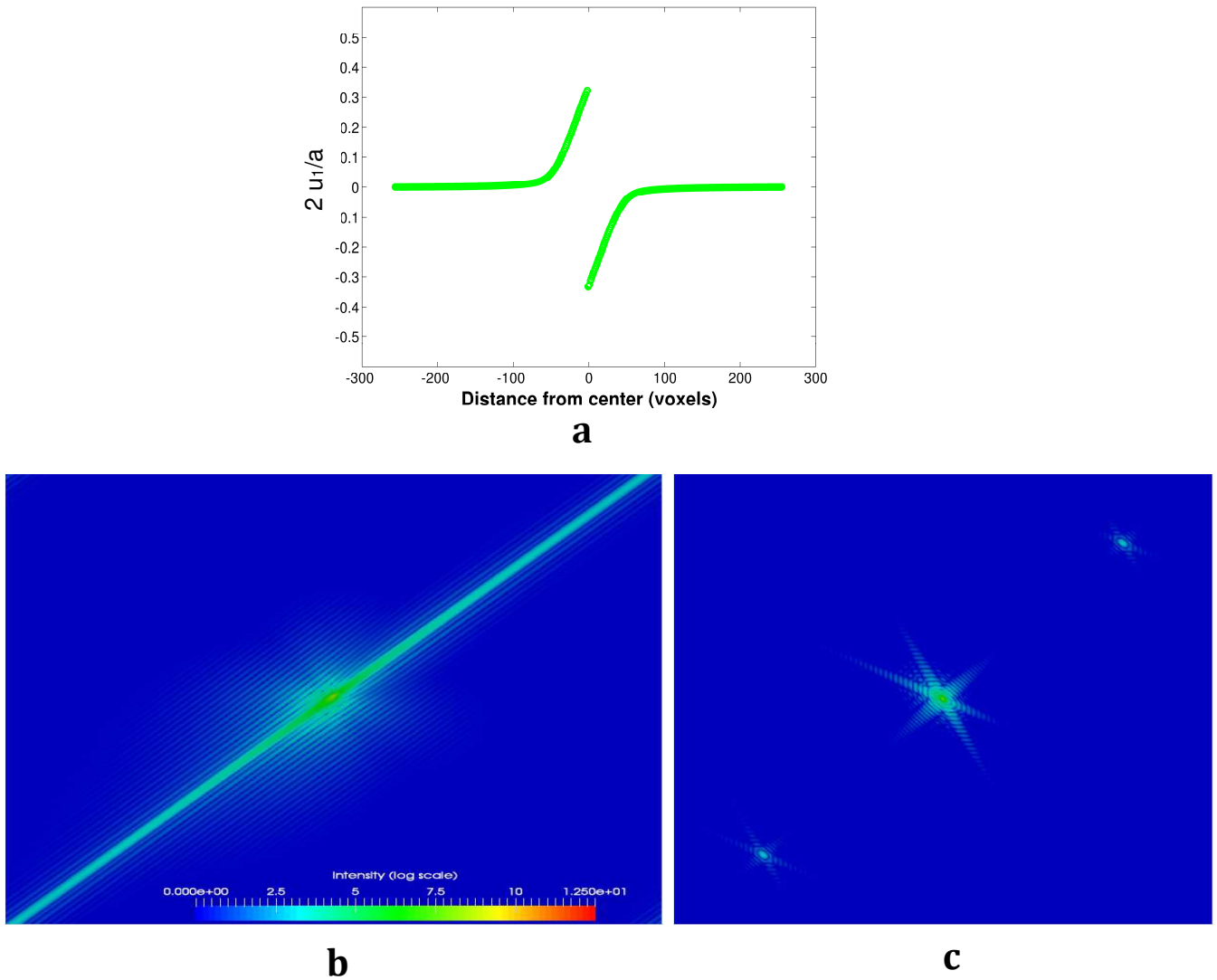


*Figure 5: 1 D plot of the corrected displacement field of a faulted dislocation loop (a), and 2D plots of the diffracted intensity. The intensities are plotted in the  $(0\bar{1}1)$  plane (b) and the  $(111)$  plane (c).*

### 4.3 1D profiles

The 3D intensity is now summed in the planes perpendicular to the  $\mathbf{G}$  vector. This allows the study of 3D data on 1D profiles. Figure 6(a) shows 1D profiles of the intensity in the case of single dislocation loop for which the displacement field is computed with the different methods discussed above.

The peak shape near the top of the peaks is the same in all cases (except a bump on the left side for the profile computed with the classical Green operator). Their long-range behavior is however quite different. When the displacement field has been calculated with the usual truncated operator (black line), a phantom peak is observed which is due to the short period oscillations near the displacement field discontinuity (Figure 1a). The behavior of the peak calculated with the modified Green operator (blue curve) is only slightly better. When the intensity has been calculated with the sub voxel patch (red curve) the long-range intensity follows the expected intensity law  $I \sim q^{-3}$  [29,30].

We now consider 64 hexagonal dislocation loops with the same  $(111)$  plane and Burgers vector distributed at random positions in the unit cell. The dislocation density is  $\sim 3.8 \times 10^{13} m^{-2}$ . Figure



6(b) compares the 1D profiles computed for both configurations (single dislocation loop and randomly distributed dislocation loop). A decrease of the maximum intensity and a broadening of the top of the peak are observed in the second configuration. However, the tails of the peak still follow the  $I \sim q^{-3}$  law and their intensity has been multiplied by 64: the tail intensity is proportional to the dislocation density. Figure 6(c) compares the 1D profiles due to a perfect (red) and faulted (green) hexagonal dislocation loop. The top of the profile is thinner for the faulted loop (factor: 2/3), but the main difference is visible at the tail which follows a  $I \sim q^{-2}$  law. It may be remarked that, as in f.c.c. metals perfect dislocations are split into two partial dislocations (Shockley partials) linked by a stacking fault, this  $q^{-2}$  tail should also be visible, but with a very low intensity.

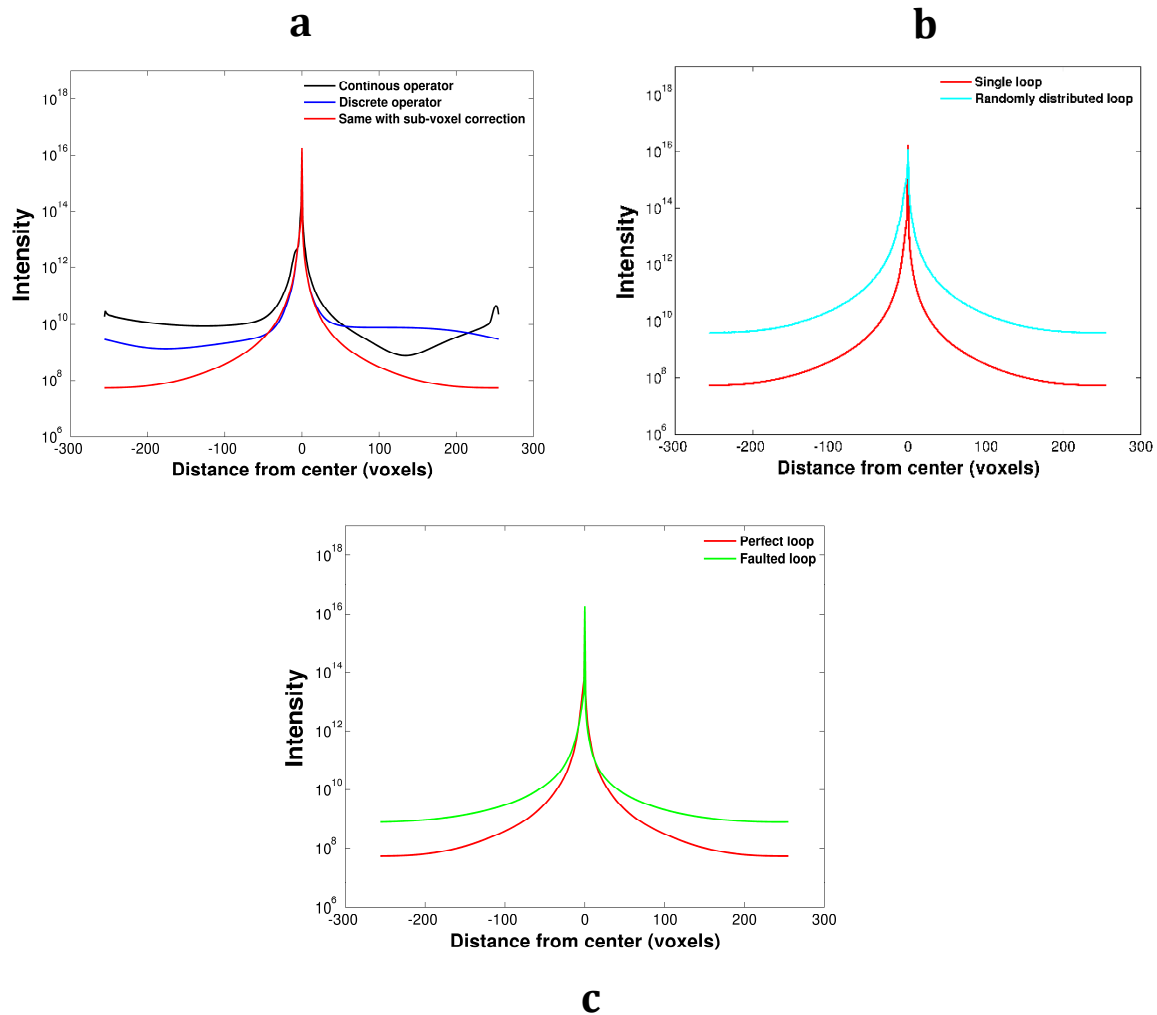


*Figure 6: 1D peak profiles computed for one dislocation loop using the different methods described in paragraph 3 (a), for a single dislocation loop and a random distribution of identical dislocation loops (b), a single perfect and faulted dislocation loop (c).*

## 5 Concluding remarks

As seen above using an FFT-based micromechanical method is a very efficient way to compute the displacement field within a voxelized representative volume of a material containing a single defect or a large number of defects, then to model the distribution of intensities near a  $\mathbf{G}$ -vector defined in the reciprocal lattice. However, this method has well-known drawbacks, such as the Gibbs phenomenon and

the consequences of the voxelization of the microstructure, such as dangling voxels [18]. Two corrections are needed: a modification of elastic Green operators [20] and a correction of the displacement field in the vicinity of transformed voxels [21]. The forms of the found discrete Green operators are different from [28]. As the modification of the operators theoretically requires a 3D sum on the whole reciprocal space, it may be expensive in CPU time (parallel computing is needed). Fortunately, it needs to be computed only once for a given set of elastic constants and then it is stored for further computations. The final correction of the displacement field seems to give good results for lattice planes with low indices within the reference frame of the representative volume, but may be difficult to implement for plane with high indices, which will occur in the simulation of polycrystalline plasticity.

The simulated peaks exhibit the main features expected from diffraction peaks from a material containing dislocations: a broad and asymmetric maximum (proportional to the Burgers vector of the dislocation loops and depending on the number and sign of the loops), a streak perpendicular to the dislocation loop plane, and a symmetry which reflects the shape of the loops. After summing the intensities in order to obtain a 1D profile which may be compared to a simple  $(\theta, 2\theta)$  diagram, we have obtained realistic shapes with tails following the expected laws:  $q^{-3}$  for perfect dislocations (due to the distribution of strain near the dislocation cores), and  $q^{-2}$  for stacking faults. If we do not take into account the voxel with the highest intensity (which would anyway be smeared in real cases), the calculated diffracted intensities span six orders of magnitude: this is larger than the peak to background ratio of most experiments.

Lastly, the present method seems to be well adapted to simulate the diffraction pattern of volume elements with a mesoscopic (micrometer) size, as the full width at half maximum of the peaks is a few tens of voxels and the background level is reached at a few hundred voxels from the maximum.

## References

1. Tréhorel, R.; Ribarik, G.; Schenk, T.; Jacques, A. Real time study of transients during high temperature creep of a Ni-based superalloy by far field high energy synchrotron X-rays diffraction. *J. Appl. Cryst.* (2018). 51, 1274-1282 <https://doi.org/10.1107/S1600576718010014>
2. Tréhorel, R. Comportement mécanique haute température du superalliage monocristallin AM1: Etude in-situ par une nouvelle technique de diffraction en rayonnement synchrotron, Université de Lorraine: Nancy, France, 2018.
3. Graverend, J.-B.L.; Dirand, L.; Jacques, A.; Cormier, J.; Ferry, O.; Schenk, T.; Gallerneau, F.; Kruch, S.; Mendez, J. In Situ Measurement of the  $\gamma/\gamma'$  Lattice Mismatch Evolution of a Nickel-Based Single-Crystal Superalloy During Non-isothermal Very High-Temperature Creep Experiments. *Metall and Mat Trans A* **2012**, 43, 3946–3951.
4. Robinson, I.; Harder, R. Coherent X-ray diffraction imaging of strain at the nanoscale. *Nat Mater* **2009**, 8, 291–298.
5. Balogh, L.; Ribárik, G.; Ungár, T. Stacking faults and twin boundaries in fcc crystals determined by x-ray diffraction profile analysis. *Journal of applied physics* **2006**, 100, 023512.
6. Ungár, T. Strain Broadening Caused by Dislocations Available online: <https://www.scientific.net/MSF.278-281.151> (accessed on Jun 16, 2018).
7. Groma, I. X-ray line broadening due to an inhomogeneous dislocation distribution. *Physical Review B* **1998**, 57, 7535.
8. Ungár, T.; Gubicza, J.; Ribárik, G.; Borbély, A. Crystallite size distribution and dislocation structure determined by diffraction profile analysis: principles and practical application to cubic and hexagonal crystals. *Journal of applied crystallography* **2001**, 34, 298–310.
9. Vaxelaire, N.; Proudhon, H.; Labat, S.; Kirchlechner, C.; Keckes, J.; Jacques, V.; Ravy, S.; Forest, S.; Thomas, O. Methodology for studying strain inhomogeneities in polycrystalline thin films during in situ thermal loading using coherent x-ray diffraction. *New J. Phys.* **2010**, 12, 035018.

10. Jacques, A. From Modeling of Plasticity in Single-Crystal Superalloys to High-Resolution X-rays Three-Crystal Diffractometer Peaks Simulation. *Metallurgical and Materials Transactions A* **2016**, *47*, 5783–5797.
11. Miller, M.P.; Dawson, P.R. Understanding local deformation in metallic polycrystals using high energy X-rays and finite elements. *Current Opinion in Solid State & Materials Science* **2014**, *5*, 286–299.
12. Demir, E.; Park, J.-S.; Miller, M.P.; Dawson, P.R. A computational framework for evaluating residual stress distributions from diffraction-based lattice strain data. *Computer Methods in Applied Mechanics and Engineering* **2013**, *265*, 120–135.
13. Hofmann, F.; Song, X.; Jun, T.-S.; Abbey, B.; Peel, M.; Daniels, J.; Honkimäki, V.; Korsunsky, A.M. High energy transmission micro-beam Laue synchrotron X-ray diffraction. *Materials Letters* **2010**, *64*, 1302–1305.
14. Song, X.; Xie, M.; Hofmann, F.; Jun, T.S.; Connolley, T.; Reinhard, C.; Atwood, R.C.; Connor, L.; Drakopoulos, M.; Harding, S. Residual stresses in linear friction welding of aluminium alloys. *Materials & Design* **2013**, *50*, 360–369.
15. Moulinec, H.; Suquet, P. A numerical method for computing the overall response of nonlinear composites with complex microstructure. *Computer Methods in Applied Mechanics and Engineering* **1998**, *157*, 69–94.
16. Moulinec, H.; Suquet, P. Fast numerical method for computing the linear and nonlinear properties of composites. *Comptes Rendus de l'Académie des Sciences. Série II* **1994**, *318*, 1417–1423.
17. Berbenni, S.; Taupin, V.; Djaka, K.S.; Fressengeas, C. A numerical spectral approach for solving elasto-static field dislocation and g-disclination mechanics. *International Journal of Solids and Structures* **2014**, *51*, 4157–4175.
18. Anglin, B.S.; Lebensohn, R.A.; Rollett, A.D. Validation of a numerical method based on Fast Fourier Transforms for heterogeneous thermoelastic materials by comparison with analytical solutions. *Computational Materials Science* **2014**, 209–217.
19. Lebensohn, R.A.; Rollett, A.D.; Suquet, P. Fast fourier transform-based modeling for the determination of micromechanical fields in polycrystals. *JOM* **2011**, *63*, 13–18.
20. Eloh, K.S.; Jacques, A.; Berbenni, S. Development of a new consistent discrete Green operator for FFT-based methods to solve heterogeneous problems with eigenstrain. *International Journal of Plasticity* **2019**, *116*, 1–23.
21. Eloh, K.S.; Jacques, A.; Ribarik, G.; Berbenni, S. The Effect of Crystal Defects on 3D High-Resolution Diffraction Peaks: A FFT-Based Method. *Materials* **2018**, *11*, No. 1669.
22. Vartanyants, I.A.; Yefanov, O.M. Coherent X-ray Diffraction Imaging of Nanostructures. *arXiv:1304.5335 [cond-mat]* **2013**.
23. Takagi, S. A Dynamical Theory of Diffraction for a Distorted Crystal. *Journal of the Physical Society of Japan* **1969**, *26*, 1239–1253.
24. Takagi, S.; IUCr Dynamical theory of diffraction applicable to crystals with any kind of small distortion Available online: <https://scripts.iucr.org/cgi-bin/paper?a03704> (accessed on Jun 19, 2018).
25. Mura, T. *Micromechanics of Defects in Solids; Mechanics of Elastic and Inelastic Solids*; 2nd ed.; Springer Netherlands, 1987; ISBN 978-90-247-3256-2.
26. Li, Q.; Anderson, P.M. A Compact Solution for the Stress Field from a Cuboidal Region with a Uniform Transformation Strain. *Journal of Elasticity* **2001**, *64*, 237–245.
27. Anderson: Crystal-based plasticity - Google Scholar Available online: [https://scholar.google.com/scholar\\_lookup?title=Crystal-based+plasticity&author=P.+M.+Anderson&publication\\_year=1995](https://scholar.google.com/scholar_lookup?title=Crystal-based+plasticity&author=P.+M.+Anderson&publication_year=1995) (accessed on Sep 5, 2018).
28. Brisard, S.; Dormieux, D. FFT-based methods for the mechanics of composites: A general variational framework. *Computational Materials Science* **2010**, *49*, 663–671.
29. Krivoglaz, M.A. *Theory of X-Ray and Thermal Neutron Scattering by Real Crystals*; Springer US, 1969; ISBN 978-1-4899-5584-5.
30. Ungár, T. Microstructural parameters from X-ray diffraction peak broadening. *Scripta Materialia* **2004**, *51*, 777–781.